

RESEARCH

Open Access



# The earliest known artificial synthesized $\epsilon$ -Fe<sub>2</sub>O<sub>3</sub> in the Deqing Kiln ceramic ware of Tang Dynasty

Gen Li<sup>1</sup>, Zhifang Wang<sup>2</sup>, Jianzhong Zhou<sup>3</sup>, Baoqiang Kang<sup>1</sup>, Yinzhou Ding<sup>1</sup>, Ming Guan<sup>1</sup>, Xiangjun Wei<sup>4\*</sup> and Yong Lei<sup>1\*</sup>

## Abstract

Metastable  $\epsilon$ -Fe<sub>2</sub>O<sub>3</sub> was discovered on a ceramic ware of Deqing kiln of the Tang Dynasty, which coexists with  $\alpha$ -Fe<sub>2</sub>O<sub>3</sub> in the brown area between adjacent black glaze areas, and it is the earliest known artificially synthesized  $\epsilon$ -Fe<sub>2</sub>O<sub>3</sub>. Based on the composition analysis of  $\alpha$ -Fe<sub>2</sub>O<sub>3</sub>,  $\epsilon$ -Fe<sub>2</sub>O<sub>3</sub> and the glass phase around them, it is speculated that some Fe<sup>3+</sup> ions were replaced by Al<sup>3+</sup> ions during the formation of  $\epsilon$ -Fe<sub>2</sub>O<sub>3</sub>, and a relatively low CaO content may be required for its crystallization. This work may promote researchers' understanding of  $\epsilon$ -Fe<sub>2</sub>O<sub>3</sub> crystals, and provide clues for the artificial synthesis of large  $\epsilon$ -Fe<sub>2</sub>O<sub>3</sub> crystals.

**Keywords**  $\epsilon$ -Fe<sub>2</sub>O<sub>3</sub>, Raman spectrum, SEM-EDS, Deqing Kiln

## Introduction

As an isomer of iron oxide,  $\epsilon$ -Fe<sub>2</sub>O<sub>3</sub> has several excellent properties such as ferromagnetic resonance in the millimeter wave band [1] and can be used as millimeter wave absorber when doped with Ga or Al [2, 3]. The most impressive is its high coercive field, which can be exceeding 2 T for pure  $\epsilon$ -Fe<sub>2</sub>O<sub>3</sub> [4, 5], and even be as high as 45kOe when doped with Rh [6, 7], making it a promising magnetic recording material. However,  $\epsilon$ -Fe<sub>2</sub>O<sub>3</sub> is a metastable phase, which will spontaneously transform into the stable  $\alpha$ -Fe<sub>2</sub>O<sub>3</sub> when crystal size exceeds 50 nm or the

temperature is high enough [8–10]. After it was first discovered in 1934 [11], researchers were not able to synthesize it artificially until 1963 [12]. Using mesoporous SiO<sub>2</sub> as the matrix is the preferred synthesizing method [10, 13–17], others such as synthesizing it in solution without matrix [18] or by pulsed laser deposition [19, 20] are also used.

Surprisingly, the recent upsurge of research on  $\epsilon$ -Fe<sub>2</sub>O<sub>3</sub> actually originated from ancient ceramics, a research field that seems to have little relationship with modern chemical synthesis. In fact, the first dendrites  $\alpha$ -Fe<sub>2</sub>O<sub>3</sub> in black spots of porcelains was found by Colomban and Sagon in a Vietnamese blue-and-white stoneware in 2004 [21], but the observation of  $\epsilon$ -Fe<sub>2</sub>O<sub>3</sub> in ancient ceramics was mainly in the past 10 years. In 2012, Liu et al. found nano-scale  $\epsilon$ -Fe<sub>2</sub>O<sub>3</sub> crystals in black-glaze ceramic shard unearthed from Qingliangsi kiln site [22]. In 2014, Dejoie et al. found iron oxide crystals up to several micrometers in hare's fur strips and oil spot patterns on black-glaze Jian wares of Song Dynasty in Fujian Province, and confirmed that they are metastable phases  $\epsilon$ -Fe<sub>2</sub>O<sub>3</sub> [23]. These findings ignite the research upsurge of  $\epsilon$ -Fe<sub>2</sub>O<sub>3</sub> in ancient ceramics.

\*Correspondence:  
Xiangjun Wei  
weixiangjun@sinap.ac.cn  
Yong Lei  
leiyong@dpm.org.cn

<sup>1</sup> Department of Conservation Science and Technology, The Palace Museum, Beijing 100009, People's Republic of China

<sup>2</sup> Renishaw (Shanghai) Trading Company Ltd. Beijing Branch Office, Zone C, Building No.6, Dian Tong Creative Square, No. 7 Jiuxianqiao North Street, Chaoyang District, Beijing 100015, China

<sup>3</sup> Deqing County Museum, Deqing, Huzhou, Zhejiang Province, China

<sup>4</sup> Shanghai Advanced Research Institute, Shanghai Synchrotron Radiation Facility, Chinese Academy of Sciences, Shanghai, China

Since then, micrometer-scale  $\epsilon$ -Fe<sub>2</sub>O<sub>3</sub> crystals in different ancient ceramics were found in the oil drop ware of Xiao kiln in Anhui Province [24], in the brown green glaze ware of Changsha kiln [25], in the purple-gold glaze of the Qing Dynasty [26], in the brown glaze of Yaozhou kiln of the Northern Song Dynasty [27–29], in the black glaze and brown glaze of Qingliangsi kiln in Baofeng, Henan [30] and in the Jingdezhen bluish white porcelain of the Song Dynasty [31]. Hoo et al. even found submillimeter-scale  $\epsilon$ -Fe<sub>2</sub>O<sub>3</sub> crystals [32]. These  $\epsilon$ -Fe<sub>2</sub>O<sub>3</sub> crystals are mainly large feathery dendrites located on the glaze surface, as well as nanometer-scale small crystals located tens of micrometer below the glaze surface. But recently, Kusano et al. revealed that  $\epsilon$ -Fe<sub>2</sub>O<sub>3</sub> crystals can also exist on the surface of unglazed stoneware under proper conditions [33]. In addition, Wang et al. studied the three-dimensional microstructure of  $\epsilon$ -Fe<sub>2</sub>O<sub>3</sub> crystals [34]. Guan et al. studied the microstructure difference of  $\epsilon$ -Fe<sub>2</sub>O<sub>3</sub> crystals in Jian wares with different colors [35]. However, even on the basis of so many examples, modern chemists have not yet successfully synthesized micrometer-scale  $\epsilon$ -Fe<sub>2</sub>O<sub>3</sub> crystals. Our understanding of  $\epsilon$ -Fe<sub>2</sub>O<sub>3</sub> in a silicate system, namely ancient ceramic glaze, maybe is still far from enough and complete. If more samples with different  $\epsilon$ -Fe<sub>2</sub>O<sub>3</sub> morphologies can be obtained, we may be able to get new inspiration on this issue.

A recently discovered Deqing ceramic ware is an interesting example. It is generally believed that Deqing kiln was created in the Eastern Han Dynasty, and its ceramic production continued until the late Tang Dynasty. It is a ceramic kiln with a long history and a unique system [36], and the latest archaeological work in the Deqing area even found the kiln sites of Shang and Zhou Dynasties [37]. With Deqing as the center, Deqing kilns are mainly distributed in the north of Zhejiang, including Yuhang, Huzhou and other places, and are famous for celadon and black ceramic products [37, 38]. The black glaze ceramic sample was unearthed from the Deqing kiln site (Deqing County, Zhejiang Province), as shown in Fig. 1a. It is speculated that its firing time was the Tang Dynasty (618–907 AD), which makes it the earliest known ceramic sample containing  $\epsilon$ -Fe<sub>2</sub>O<sub>3</sub> crystals. The  $\epsilon$ -Fe<sub>2</sub>O<sub>3</sub> crystals are not located on the surface of the black glaze, but coexist with  $\alpha$ -Fe<sub>2</sub>O<sub>3</sub> in the brown area between adjacent black glaze areas. Such a phenomenon is quite similar to the  $\epsilon$ -Fe<sub>2</sub>O<sub>3</sub> and  $\alpha$ -Fe<sub>2</sub>O<sub>3</sub> crystals on the surface of traditional Japanese Bizen stoneware [33, 39], and  $\alpha$ -Fe<sub>2</sub>O<sub>3</sub> in the ‘Huoshihong’ regions on the blue-and-white porcelain of the Yuan Dynasty [40].

In this paper, we will carefully investigate the  $\epsilon$ -Fe<sub>2</sub>O<sub>3</sub> and  $\alpha$ -Fe<sub>2</sub>O<sub>3</sub> crystals on the sample surface, analyze the spatial distribution of these two phases and the elemental compositions of different surface areas, and then try to

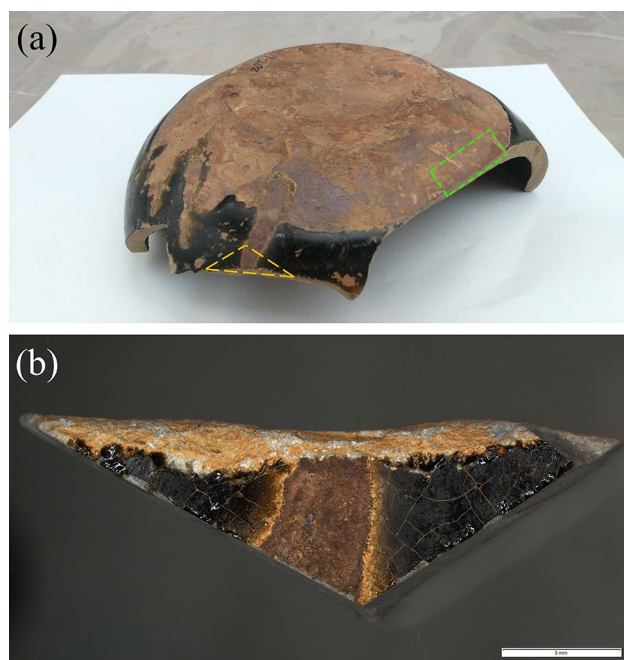


**Fig. 1** The ceramic ware of Deqing Kiln and the sample used in our work. **a** The original ceramic ware. The sample used for observation is shown by the orange triangle, and the sample used in thermal expansion experiments is shown by the green rectangular. **b** The optical image of the sample, where the scale bar is 5 mm

discuss the possible formation mechanism and improve our understanding of  $\epsilon$ -Fe<sub>2</sub>O<sub>3</sub> phase. The sample used in our experiments is shown in Fig. 1b, and its position on the original ceramic ware is marked by the yellow triangle in Fig. 1a.

## Methods

The Raman spectra were obtained by Renishaw inVia laser confocal microscope. In our experiments, the laser wavelength used was 785 nm, laser power was 5mW, optical grating type was 1200 l/mm, and single point testing time was 10 s. Streamline technique was used in the detection of Raman signal. The spot size used in single point testing was roughly  $1 \times 20 \mu\text{m}^2$ , and the spot size used in Raman mapping was roughly  $1 \times 40 \mu\text{m}^2$ .

The XRD spectrum was obtained by Bruker D8 DISCOVER X-ray diffractometer. The X-ray used was Co-K $\alpha$  with a wavelength of 0.178897 nm, and the minimum spot size was about 400  $\mu\text{m}$ .

The micromorphology observation was conducted by MIRA3 field-emission scanning electron microscope (FE-SEM, TESCAN) equipped with EDS accessory (Genesis, EDAX, USA). Before observation, carbon layer with a thickness of about 10 nm was deposited to enhance the surface conductivity. In our experiments, back-scattering electron (BSE) detector was used, the accelerating voltage

was 25 kV, the beam intensity used in imaging and EDS was 12 and 18 respectively, the corresponding spot size was about 5 nm and 40 nm, and the single point testing time for EDS analysis was 120 s.

The ceramic ware body's thermal expansion curve was measured by DIL402C thermal expansion meter of NETZSCH. In our experiments, the sample size was 25 mm × 5 mm × 5 mm, the heating rate was 5 °C/min, the sweep gas was nitrogen gas with a flow rate of 50 mL/min.

## Results and discussion

### Macroscopic information

Figure 2a shows the XRD spectrum of the brown area in the sample. Figure 2b shows the thermal expansion curve measured by push-rod thermal expansion method, and its firing temperature can be calculated to be  $1180 \pm 20$  °C [41, 42]. The optical image and SEM back-scattering image of this sample are shown in Fig. 2c and d.

Through comparison with the database, we found that there were various phases in the analyzed region such as quartz, mullite  $\epsilon$ -Fe<sub>2</sub>O<sub>3</sub> and  $\alpha$ -Fe<sub>2</sub>O<sub>3</sub>. Compared with pure  $\epsilon$ -Fe<sub>2</sub>O<sub>3</sub>, Al-doped  $\epsilon$ -Fe<sub>2</sub>O<sub>3</sub> (the reference phase in the database is Fe<sub>1.71</sub>Al<sub>0.24</sub>Mg<sub>0.02</sub>Ti<sub>0.03</sub>O<sub>3</sub>, which was found in the ore) seems to be in better agreement with the experimental peak positions. It should be noted that we do not intend to claim the existence of Fe<sub>1.71</sub>Al<sub>0.24</sub>Mg<sub>0.02</sub>Ti<sub>0.03</sub>O<sub>3</sub> in this sample, but only want to use it as evidence that the substitution of Al<sup>3+</sup> into original  $\epsilon$ -Fe<sub>2</sub>O<sub>3</sub> will decrease the crystal lattice constants, and fit better with minor peaks in the experimental XRD spectrum.

It can be found in Fig. 2c and d that the background color of the brown area is dark brown, the boundary between brown area and the black glaze is bright orange, while there are many red brown regions in the brown area, whose brightness in the back-scattering image is significantly higher than the background, so it can be speculated that the iron concentrations in these regions are very high.

### Typical crystal morphologies

Figure 3 shows the typical morphologies of the crystals in the sample and their Raman spectra. In Fig. 3e, four typical Raman peaks of  $\epsilon$ -Fe<sub>2</sub>O<sub>3</sub> crystals locate near 91 cm<sup>-1</sup>, 124 cm<sup>-1</sup>, 156 cm<sup>-1</sup> and 238 cm<sup>-1</sup> [29], which are indicated by green dash lines; four typical Raman peaks of  $\alpha$ -Fe<sub>2</sub>O<sub>3</sub> crystals locate near 225 cm<sup>-1</sup>, 295 cm<sup>-1</sup>, 410 cm<sup>-1</sup> and 612 cm<sup>-1</sup> [43, 44], which are indicated by red dash lines. It can be seen that the white feathery dendrites in 3(a) are  $\epsilon$ -Fe<sub>2</sub>O<sub>3</sub>, which are located at the border between brown area and black glaze; the coarse granular crystals in 3(b) are located in the brown area, which are

also  $\epsilon$ -Fe<sub>2</sub>O<sub>3</sub>. The peak at about 295 cm<sup>-1</sup> in spectrum (a) was lost in spectrum (b), which may be related to spinel phases such as maghemite and magnetite [44].

However, although the coarse and fine granular crystals at the center of 3(c) and 3(d) look very similar to that in 3(b), Raman spectra proved that they are  $\alpha$ -Fe<sub>2</sub>O<sub>3</sub>, which indicates that these two phases cannot be distinguished simply according to the morphologies. It should be noted that the width of peaks at 225 cm<sup>-1</sup> and 295 cm<sup>-1</sup> are broader than that of pure  $\alpha$ -Fe<sub>2</sub>O<sub>3</sub> crystals in the literature, which suggests that the Al<sup>3+</sup> ion may substitute into the lattice of  $\alpha$ -Fe<sub>2</sub>O<sub>3</sub> crystals [44].

### Phase mapping

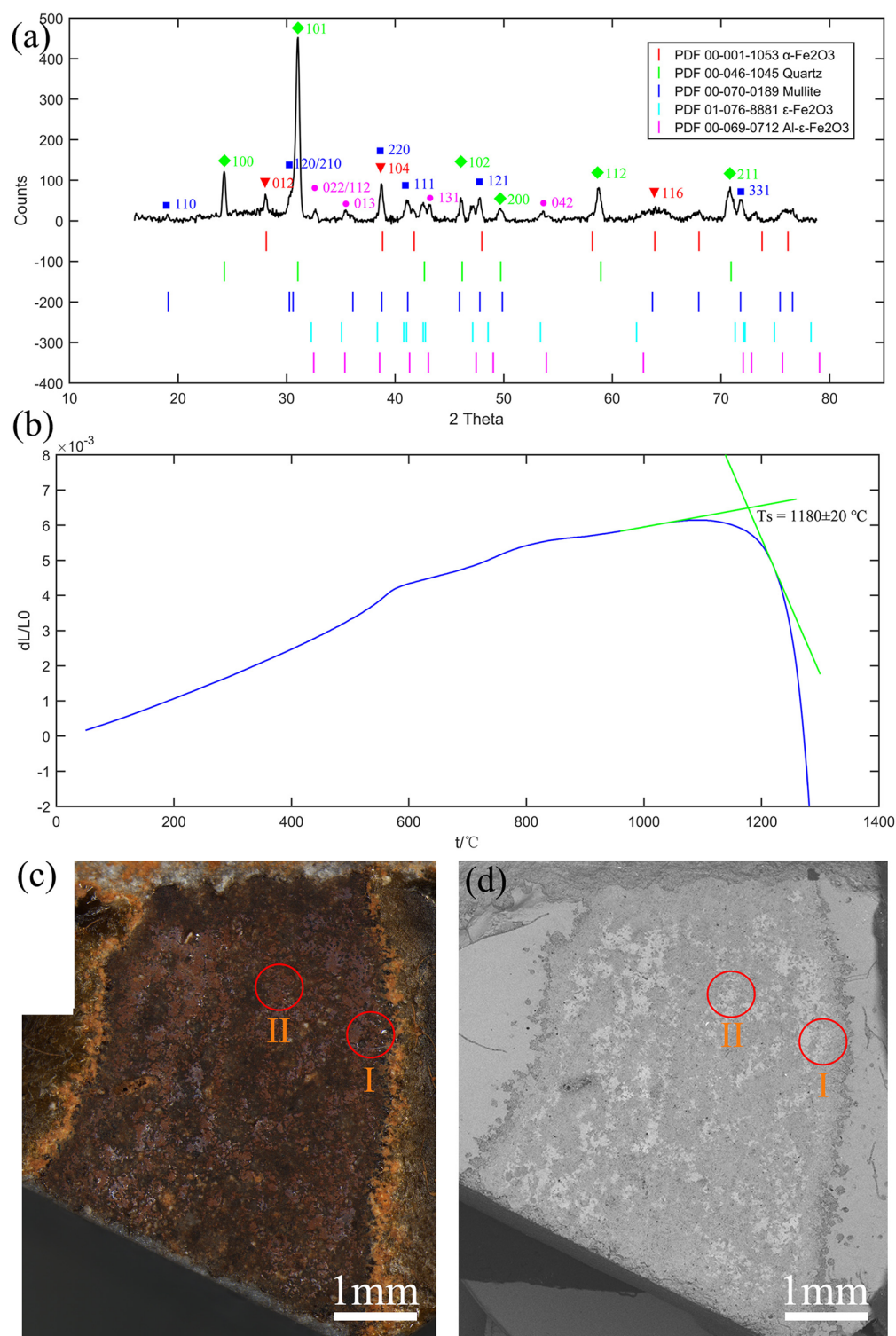
In order to verify the distributions of  $\epsilon$ -Fe<sub>2</sub>O<sub>3</sub> and  $\alpha$ -Fe<sub>2</sub>O<sub>3</sub>, Raman mappings were conducted by micro-Raman spectrometer in region I and region II, as shown in Fig. 4 and Fig. 5. After collecting the Raman spectra of each point, the software would automatically calculate and extract the principal components, which correspond to different phases.

Figure 4 shows the local Raman mapping result of region I. The first four of the six principal components calculated correspond to the Raman spectra of  $\alpha$ -Fe<sub>2</sub>O<sub>3</sub>,  $\epsilon$ -Fe<sub>2</sub>O<sub>3</sub>, quartz and anatase respectively, as shown in Fig. 4c. The phases correspond to the other two unknown principal components are not directly given by database, but unknown 1 is probably a luminescence due to the presence of rare earths [43]. Comparing Fig. 4b and d, it can be seen that  $\alpha$ -Fe<sub>2</sub>O<sub>3</sub> and  $\epsilon$ -Fe<sub>2</sub>O<sub>3</sub> coexist in this region with irregular morphologies, and  $\alpha$ -Fe<sub>2</sub>O<sub>3</sub> looks brighter than  $\epsilon$ -Fe<sub>2</sub>O<sub>3</sub> in the bright-field image.

Figure 5 shows the local Raman mapping result of region II. The three principal components calculated correspond to  $\alpha$ -Fe<sub>2</sub>O<sub>3</sub>,  $\epsilon$ -Fe<sub>2</sub>O<sub>3</sub> and quartz respectively, as shown in Fig. 5c. It can be seen from Fig. 5b and d that  $\alpha$ -Fe<sub>2</sub>O<sub>3</sub> is still brighter than  $\epsilon$ -Fe<sub>2</sub>O<sub>3</sub>.

### Compositions of typical areas

Now, we have roughly clarified the morphologies and distributions of  $\alpha$ -Fe<sub>2</sub>O<sub>3</sub> and  $\epsilon$ -Fe<sub>2</sub>O<sub>3</sub>. In order to obtain the clues of its formation mechanism, it is necessary to analyze the compositions of these phases and their surrounding materials. For this reason, we chose a series of testing positions to acquire the EDS spectra of  $\alpha$ -Fe<sub>2</sub>O<sub>3</sub> (PA), glass phase around  $\alpha$ -Fe<sub>2</sub>O<sub>3</sub> (GA),  $\epsilon$ -Fe<sub>2</sub>O<sub>3</sub> (PE), glass phase around  $\epsilon$ -Fe<sub>2</sub>O<sub>3</sub> (GE), large feathery dendrites  $\epsilon$ -Fe<sub>2</sub>O<sub>3</sub> (FE), glass phase around the large feathery dendrites  $\epsilon$ -Fe<sub>2</sub>O<sub>3</sub> (GF), common glass phase (CG), glaze (G) and body (B) on the sample surface. Several typical test areas have been marked in Figs. 3, 4 and 5, while polished cross-section samples were used to test the compositions of glaze and body. After statistical data processing, the



**Fig. 2** The XRD spectrum of the sample's brown area, the thermal expansion curve, and the schematic diagram of the experimental regions in this paper. **a** The experimental XRD spectrum. The peak positions of relevant phases are shown by different symbols and the Miller indexes are labeled. Here the red, green, blue, cyan and magenta stand for  $\alpha$ -Fe<sub>2</sub>O<sub>3</sub>, quartz, mullite,  $\epsilon$ -Fe<sub>2</sub>O<sub>3</sub> and Al-doped  $\epsilon$ -Fe<sub>2</sub>O<sub>3</sub>, respectively. It can be seen that the  $\epsilon$ -Fe<sub>2</sub>O<sub>3</sub> and  $\alpha$ -Fe<sub>2</sub>O<sub>3</sub> coexist here. **b** The sample's thermal expansion curve. **c** and **d** are optical and SEM back-scattering images of the sample's brown area, and the regions of the following experiments are shown by red circles

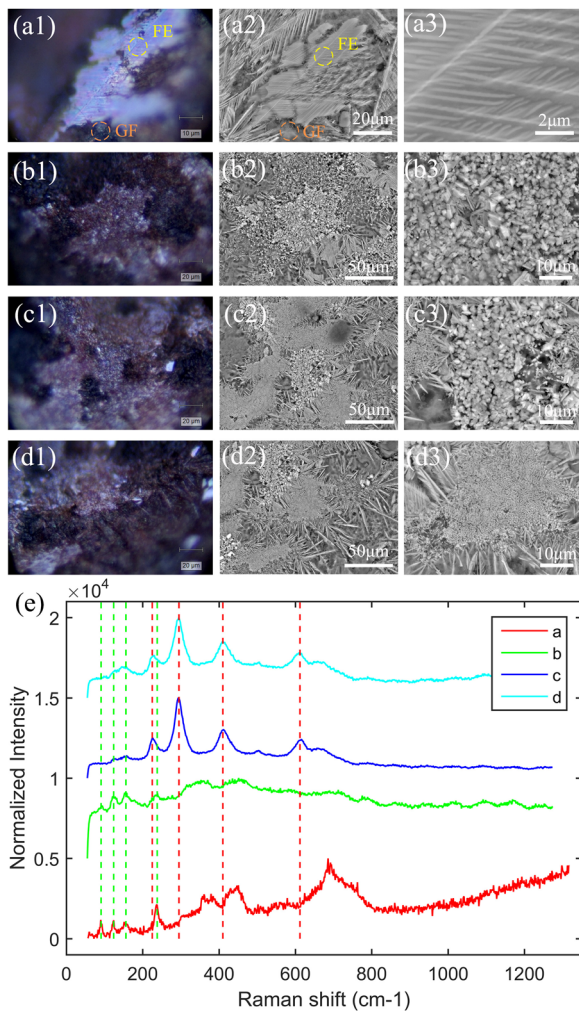


**Fig. 3** The crystal morphologies and Raman spectra in different sample regions. **a–d** come from region I in Fig. 2, and the “1”“2” and “3” in each subplot number denote optical images from Raman microscope, middle magnification SEM back-scattering images and high magnification SEM back-scattering images. **e** shows the Raman spectra obtained in the center of each subplot

experimental results are shown in Table 1, in which the uncertainty of the instrument is taken as 0.1%.

We observed that the large feathery dendrites all appeared at the boundaries between black glaze and brown area. Table 1 shows that both the SiO<sub>2</sub>/Al<sub>2</sub>O<sub>3</sub> ratio and the CaO content of large crystals and their surrounding glass phase are between the corresponding parameters of body and glaze, which is consistent with our observation above.

In the brown area, the SiO<sub>2</sub>/Al<sub>2</sub>O<sub>3</sub> ratio of α-Fe<sub>2</sub>O<sub>3</sub> (2.6) and ε-Fe<sub>2</sub>O<sub>3</sub> (2.0) are significantly lower than that of the body (3.6) and glaze (4.3), which indicates that the aluminum content is higher in the area where ε-Fe<sub>2</sub>O<sub>3</sub>

exists; the SiO<sub>2</sub>/Al<sub>2</sub>O<sub>3</sub> ratio of glass phase near large feathery dendrites (3.8) and common glass phase (4.1) are between that of the body and glaze; while the SiO<sub>2</sub>/Al<sub>2</sub>O<sub>3</sub> ratio of the glass phase near α-Fe<sub>2</sub>O<sub>3</sub> (5.8) and ε-Fe<sub>2</sub>O<sub>3</sub> (4.4) are higher than that of the body and glaze. On this basis, it can be inferred that when the iron oxide crystals were formed, the Si and Al elements in this system were redistributed, and the requirements on SiO<sub>2</sub>/Al<sub>2</sub>O<sub>3</sub> ratio of ε-Fe<sub>2</sub>O<sub>3</sub> (2.0) is more stringent. If we simply assume that the crystallization of Fe<sub>2</sub>O<sub>3</sub> will affect the element distribution in the glass phase, it will be difficult to explain the selectivity to aluminum shown by α-Fe<sub>2</sub>O<sub>3</sub> and ε-Fe<sub>2</sub>O<sub>3</sub>.

As mentioned in “Macroscopic information” Section, compared with pure ε-Fe<sub>2</sub>O<sub>3</sub>, doped ε-Fe<sub>2</sub>O<sub>3</sub> (the chemical formula of the reference material in the database is Fe<sub>1.71</sub>Al<sub>0.24</sub>Mg<sub>0.02</sub>Ti<sub>0.03</sub>O<sub>3</sub>) seems to fit better with the experimental spectrum. According to the silicon-aluminum ratios in different regions given by EDS, it is natural to speculate that some Fe<sup>3+</sup> may be substituted by Al<sup>3+</sup> in ε-Fe<sub>2</sub>O<sub>3</sub> phase. The radius of Al<sup>3+</sup> is 50 pm, which is slightly smaller than that of Fe<sup>3+</sup> (60 pm), and they both carry the same number of positive charges, therefore in theory Al<sup>3+</sup> can enter the lattice of Fe<sub>2</sub>O<sub>3</sub>. In fact, in another work of ours to be published, it has been confirmed by DFT calculation that the lattice of ε-Fe<sub>2-x</sub>Al<sub>x</sub>O<sub>3</sub> indeed exist stably, and the corresponding apparent color changes due to the change of system energy level. Previous literature also reported the substitution behavior of Al and Ti atoms in α-Fe<sub>2</sub>O<sub>3</sub> crystals [25].

And then it needs to be pointed out that the crystallization of ε-Fe<sub>2</sub>O<sub>3</sub> may require a relatively low CaO content in the system. In previous literature, the content of CaO in typical black glaze with ε-Fe<sub>2</sub>O<sub>3</sub> crystallization is less than 8%, and the content of iron oxide is mostly 5–8% [24, 26, 28, 30, 35]. However, in this sample, the CaO content is less than 5% in the regions where ε-Fe<sub>2</sub>O<sub>3</sub> crystals exist. On the contrary, the CaO content of the black glaze is close to 20%. Although the Fe<sub>2</sub>O<sub>3</sub> content of the black glaze is also about 6%, there is still no ε-Fe<sub>2</sub>O<sub>3</sub> crystallization.

In addition, we found that in the brown area, the mass fraction of Fe<sub>2</sub>O<sub>3</sub> is more than 35% where α-Fe<sub>2</sub>O<sub>3</sub> and ε-Fe<sub>2</sub>O<sub>3</sub> exist, and is only about 17% where the large feathery dendrites ε-Fe<sub>2</sub>O<sub>3</sub> are located, which may be due to the fact that the large feathery dendrites are very thin, while the Fe<sub>2</sub>O<sub>3</sub> crystallized in the brown area are thicker. As previously reported, the Fe<sub>2</sub>O<sub>3</sub> content of large ε-Fe<sub>2</sub>O<sub>3</sub> feathery dendrites on the surface of black glaze given by SEM-EDS was also between 13 and 24% [35]. One possible explanation is that the iron crystallized in these brown areas may at least partly come from the inside of the body.

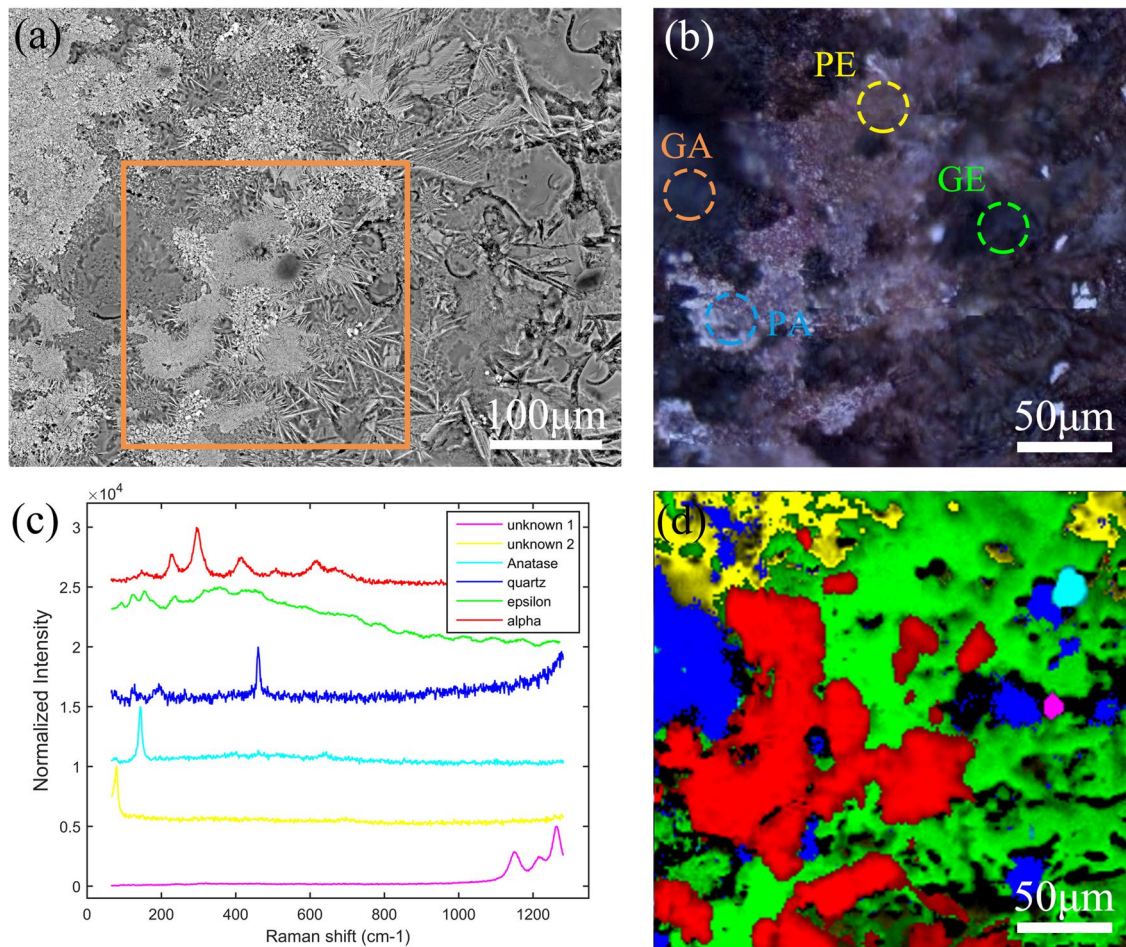


**Fig. 4** Local Raman mapping results in region I. **a** Local back-scattering SEM images in region I, where the orange square shows the Raman mapping area. **b** Optical image corresponds to the orange square area shown (a). **c** Six principal Raman components obtained in the Raman mapping of area (b). **d** Raman mapping result of (b) area. In (c) and 4(d), red, green, blue and cyan represent  $\alpha$ -Fe<sub>2</sub>O<sub>3</sub>,  $\epsilon$ -Fe<sub>2</sub>O<sub>3</sub>, quartz and anatase respectively

According to Robert Tichane's monograph *Ash Glazes*, potassium carbonate will be absorbed by bisqued body, and then react in the body to make it more vitrified and to make it give up its iron oxide to the surface. We think that this also explain the reason why the K<sub>2</sub>O content was much higher in the region of "Huoshihong" [40], and why should K<sub>2</sub>CO<sub>3</sub> be used to reproduce the brownish color on Bizen stoneware [33]. When chlorine exists in the body, the iron in the body will diffuse outward in the form of highly volatile FeCl<sub>3</sub> and gather on the surface when heated [45]. From Table 1, we can easily find that only in the areas where  $\epsilon$ -Fe<sub>2</sub>O<sub>3</sub> and  $\alpha$ -Fe<sub>2</sub>O<sub>3</sub> exist can chlorine be detected, which partly proves the rationality of the outward diffusion and aggregation mechanism of FeCl<sub>3</sub>. Moreover, the content of K<sub>2</sub>O in these two crystals and their surrounding glass phases are also higher than that in the body and glaze. We believe that it is related to the firing process of Deqing kiln.

It is generally believed that the Deqing kiln in the Tang Dynasty did not use sagger but used lamination naked firing technique [46], which inevitably made wood ash and other substances fall on the unglazed surface with the flow of high temperature air. Yin et al. had systematically studied the proto-porcelain kilns in Deqing area, and found that the glassy surface (or kiln sweat) on the inner wall has a high potassium content—the mass fraction of K<sub>2</sub>O is generally above 5%, while the mass fraction of K<sub>2</sub>O in the kiln wall fragments is only about 2% [47]. This shows that the extra K<sub>2</sub>O must have come from the wood and other fuels used. The distribution of brown areas in our sample is irregular, but most of these areas appear on the unglazed side rather than on the bottom, which is consistent with the speculation that wood ash falling increases the local potassium content.

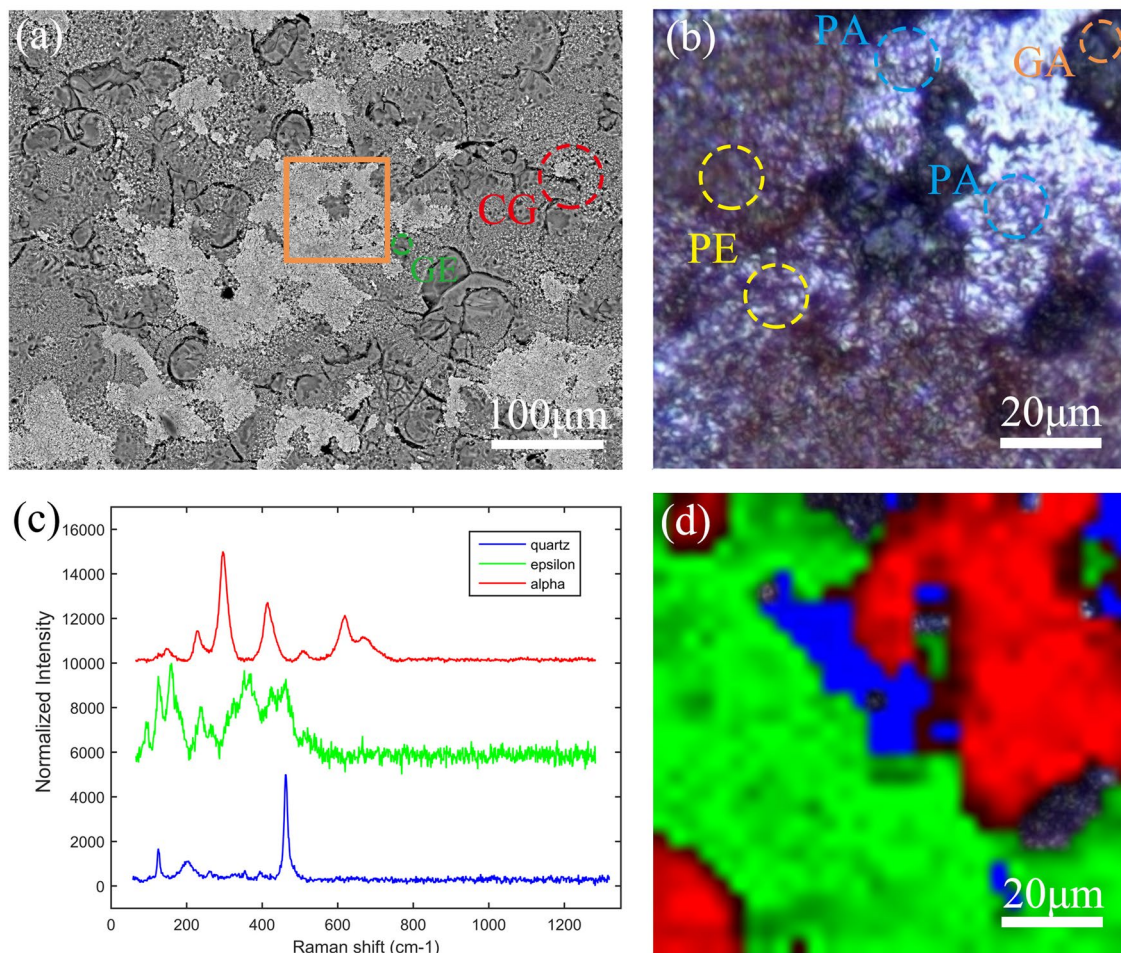


**Fig. 5** Local Raman mapping results in region II. **a** Local back-scattering SEM images in region II, where the orange square shows the Raman mapping area. **b** Optical image corresponds to the orange square area shown (a). **c** Three principal Raman components obtained in the Raman mapping of area (b). **d** Raman mapping results of (b) area. In (c) and (d), red, green and blue represent  $\alpha\text{-Fe}_2\text{O}_3$ ,  $\epsilon\text{-Fe}_2\text{O}_3$  and quartz, respectively

**Table 1** Compositions of different sample areas (wt%)

	PE	GE	PA	GA	FE	GF	CG	G	B
Na <sub>2</sub> O	2.1 ± 0.2	3.7 ± 0.5	1.9 ± 0.2	4.1 ± 0.3	1.8 ± 0.2	3.5 ± 0.4	4.5 ± 0.2	1.3 ± 0.1	2.3 ± 0.1
MgO	2.5 ± 0.4	1.2 ± 0.3	1.8 ± 0.3	1.1 ± 0.2	1.9 ± 0.1	1.8 ± 0.2	1.4 ± 0.2	2.1 ± 0.1	1.1 ± 0.1
Al <sub>2</sub> O <sub>3</sub>	17.2 ± 0.3	12.6 ± 2.4	14.2 ± 0.5	15.3 ± 1.6	14.7 ± 0.2	16.4 ± 1.3	16.0 ± 0.9	12.8 ± 0.2	19.4 ± 0.5
SiO <sub>2</sub>	34.6 ± 1.2	73 ± 5	36.7 ± 2.0	67.2 ± 2.5	54.0 ± 0.7	62.4 ± 2.8	65.3 ± 1.8	54.9 ± 0.4	69.8 ± 0.8
P <sub>2</sub> O <sub>5</sub>	0.0 ± 0.1	0.1 ± 0.1	0.0 ± 0.1	0.1 ± 0.1	0.2 ± 0.1	0.1 ± 0.1	0.1 ± 0.1	0.4 ± 0.1	0.0 ± 0.1
Cl <sub>2</sub> O	0.2 ± 0.1	0.0 ± 0.1	0.2 ± 0.1	0.0 ± 0.1	0.0 ± 0.1	0.0 ± 0.1	0.0 ± 0.1	0.0 ± 0.1	0.0 ± 0.1
K <sub>2</sub> O	4.2 ± 0.3	3.5 ± 0.6	4.2 ± 0.3	5.5 ± 0.4	4.1 ± 0.1	3.6 ± 0.5	4.8 ± 0.4	1.5 ± 0.1	2.9 ± 0.2
CaO	1.5 ± 0.1	1.2 ± 0.2	1.4 ± 0.1	1.8 ± 0.3	4.9 ± 0.4	4.8 ± 0.4	1.8 ± 0.3	19.5 ± 0.4	0.8 ± 0.1
TiO <sub>2</sub>	1.7 ± 0.1	0.6 ± 0.2	1.5 ± 0.2	1.4 ± 0.4	1.0 ± 0.1	1.1 ± 0.2	0.8 ± 0.2	0.9 ± 0.1	0.9 ± 0.1
MnO <sub>2</sub>	0.4 ± 0.1	0.1 ± 0.1	0.3 ± 0.1	0.2 ± 0.1	0.3 ± 0.1	0.3 ± 0.1	0.1 ± 0.1	0.4 ± 0.1	0.1 ± 0.1
Fe <sub>2</sub> O <sub>3</sub>	35.7 ± 1.2	3.9 ± 1.5	37.7 ± 2.0	3.4 ± 0.6	17.1 ± 0.8	5.9 ± 1.1	5.2 ± 0.9	6.1 ± 0.2	2.7 ± 0.2
SiO <sub>2</sub> /Al <sub>2</sub> O <sub>3</sub>	2.0 ± 0.1	5.8 ± 1.2	2.6 ± 0.2	4.4 ± 0.5	3.7 ± 0.1	3.8 ± 0.4	4.1 ± 0.3	4.3 ± 0.1	3.6 ± 0.1

PE  $\epsilon\text{-Fe}_2\text{O}_3$ , GE glass phase around the  $\epsilon\text{-Fe}_2\text{O}_3$ , PA  $\alpha\text{-Fe}_2\text{O}_3$ , GA glass phase around the  $\alpha\text{-Fe}_2\text{O}_3$ , FE large feathery dendrites  $\epsilon\text{-Fe}_2\text{O}_3$ , GF glass phase around the large feathery dendrites  $\epsilon\text{-Fe}_2\text{O}_3$ , CG common glass phase, G glaze, B body

However, we cannot completely rule out the possibility that these brown areas come from a thin layer of body-protective glaze [48, 49], or are formed spontaneously during the firing process. As for the growing mechanism of  $\epsilon$ -Fe<sub>2</sub>O<sub>3</sub> crystals, scholars also have not reached a consensus. Kusano et al. regarded  $\epsilon$ -Fe<sub>2</sub>O<sub>3</sub> as epitaxial product on spinel substrates such as (Mg, Fe)(Al, Fe)<sub>2</sub>O<sub>4</sub> and  $\gamma$ -Fe<sub>2</sub>O<sub>3</sub>, while Hoo et al. thought that  $\epsilon$ -Fe<sub>2</sub>O<sub>3</sub> was grown on radial mullite whiskers. These problems deserve to be further studied.

## Conclusion

The  $\epsilon$ -Fe<sub>2</sub>O<sub>3</sub> was discovered in the ceramic ware of Deqing kiln in Tang Dynasty, which is the earliest known artificially synthesized  $\epsilon$ -Fe<sub>2</sub>O<sub>3</sub>. Different from previously found large feathery dendrites  $\epsilon$ -Fe<sub>2</sub>O<sub>3</sub> on the surface of black glaze, the  $\epsilon$ -Fe<sub>2</sub>O<sub>3</sub> crystals in this sample are only located in the brown area between adjacent black glazes and coexist with  $\alpha$ -Fe<sub>2</sub>O<sub>3</sub>. By analyzing the compositions of  $\alpha$ -Fe<sub>2</sub>O<sub>3</sub>,  $\epsilon$ -Fe<sub>2</sub>O<sub>3</sub> and glass phases around them, we speculate that some Fe<sup>3+</sup> ions may have been replaced by Al<sup>3+</sup> ions during the formation of  $\epsilon$ -Fe<sub>2</sub>O<sub>3</sub> phase, and the crystallization of  $\epsilon$ -Fe<sub>2</sub>O<sub>3</sub> may require that the CaO content in the system should not be too high. In addition, the iron of  $\alpha$ -Fe<sub>2</sub>O<sub>3</sub> and  $\epsilon$ -Fe<sub>2</sub>O<sub>3</sub> in the brown area may partly come from the interior of the body. Both the potassium carbonate brought by wood ash in the kiln and FeCl<sub>3</sub> diffused outward from the body contributed to the aggregation of inner iron on the surface.

## Abbreviations

FE-SEM	Field-emission scanning electron microscope
EDS	Energy dispersive spectrometer
BSE	Back-scattering electron
XRD	X-Ray diffraction

## Acknowledgements

The authors would like to thank He Li for his help with this work, especially his profound knowledge and penetrating insight in the study of ancient ceramics. The authors also would like to thank Yueyuan Yu for her help in English writing.

## Author contributions

GL designed the research schedule, performed the experiments of SEM, analyzed data and wrote the manuscript. ZW performed the experiments of Raman. JZ provided the cultural heritage sample. BK performed the experiments of XRD. YD performed the thermal expansion experiment. MG analyzed data. XW and YL acquired the funding, reviewed and edited this manuscript. All authors read and approved the final manuscript.

## Funding

This work was financially supported by the Chinese National Natural Science Foundation (Grant Nos. U1932203).

## Availability of data and materials

The data that support the findings of this study are available from the corresponding author upon reasonable request.

## Declarations

### Competing interests

The authors declare no competing interests.

Received: 24 November 2022 Accepted: 27 February 2023

Published online: 22 March 2023

## References

- Tucek J, Zbořil R, Namai A, Ohkoshi S.  $\epsilon$ -Fe<sub>2</sub>O<sub>3</sub>: an advanced nanomaterial exhibiting giant coercive field, millimeter-wave ferromagnetic resonance, and magnetoelectric coupling. *Chem Mater*. 2010;22(24):6483–505.
- Ohkoshi S, Kuroki S, Sakurai S, Matsumoto K, Sato K, Sasaki S. A millimeter-wave absorber based on gallium-substituted epsilon-iron oxide nanomagnets. *Angew Chem Int Ed*. 2007;46(44):8392–5.
- Namai A, Sakurai S, Nakajima M, Suemoto T, Matsumoto K, Goto M, et al. Synthesis of an electromagnetic wave absorber for high-speed wireless communication. *J Am Chem Soc*. 2009;131(3):1170–3.
- Jin J, Ohkoshi S, Hashimoto K. Giant coercive field of nanometer-sized iron oxide. *Adv Mater*. 2004;16(1):48–51.
- Yoshikiyo M, Yamada K, Namai A, Ohkoshi S. Study of the electronic structure and magnetic properties of  $\epsilon$ -Fe<sub>2</sub>O<sub>3</sub>. *J Phys Chem C*. 2012;116:8688–91.
- Namai A, Yoshikiyo M, Yamada K, Sakurai S, Goto T, Yoshida T, et al. Hard magnetic ferrite with a gigantic coercivity and high frequency millimetre wave rotation. *Nat Commun*. 2012;3(1):1035–1035.
- Ohkoshi S, Imoto K, Namai A, Anan S, Yoshikiyo M, Tokoro H. Large coercive field of 45 kOe in a magnetic film based on metal-substituted  $\epsilon$ -Iron Oxide. *J Am Chem Soc*. 2017;139(38):13268–71.
- Zbořil R, Mashlan M, Petridis D. Iron (III) Oxides from thermal processes—synthesis, structural and magnetic properties, Mössbauer spectroscopy characterization, and applications. *Chem Mater*. 2002;14(3):969–82.
- Machala L, Tucek J, Zboril R. Polymorphous transformations of nanometric iron(III) oxide: a review. *Chem Mater*. 2011;23:3255–72.
- Sakurai S, Namai A, Hashimoto K, Ohkoshi S. First observation of phase transformation of all four Fe<sub>2</sub>O<sub>3</sub> phases ( $\gamma \rightarrow \epsilon \rightarrow \beta \rightarrow \alpha$ -Phase). *J Am Chem Soc*. 2009;131(51):18299–303.
- Forestier H, Guiot-Guillain G. New ferromagnetic variety of ferric oxide. *C R Acad Sci (Paris)*. 1934;199:720.
- Schrader R, Ttner G. Eine neue Eisen(III)-oxidphase:  $\epsilon$ -Fe<sub>2</sub>O<sub>3</sub>. *Z Anorg Allg Chem*. 1963;320(5–6):220–34.
- Tadic M, Spasojevic V, Kusigerski V, Markovic D, Remskar M. Formation of  $\epsilon$ -Fe<sub>2</sub>O<sub>3</sub> phase by the heat treatment. *Scr Mater*. 2008;58:703–6.
- Masubuchi Y, Sato Y, Sawada A, Motohashi T, Kiyono H, Kikkawa S. Crystallization and magnetic property of iron oxide nanoparticles precipitated in silica glass matrix. *J Eur Ceram Soc*. 2011;31(14):2459–62.
- Wang YG, Ma J, Zuo-Jiang SZ, Chen KZ. Tailorable magnetic properties of  $\epsilon$ -Fe<sub>2</sub>O<sub>3</sub>/SiO<sub>2</sub> hybrid via alkaline etching. *Ceram Int*. 2017;43(18):16482–7.
- Yakushkin SS, Balaev DA, Dubrovskiy AA, Semenov SV, Knyazev YV, Bayukov OA, et al.  $\epsilon$ -Fe<sub>2</sub>O<sub>3</sub> nanoparticles embedded in silica xerogel—Magnetic metamaterial. *Ceram Int*. 2018;44(15):17852–7.
- Knyazev YV, Yakushkin SS, Balaev DA, Dubrovsky AA, Semenov SV, Bayukov OA, et al. Magnetic properties of ultrafine  $\epsilon$ -Fe<sub>2</sub>O<sub>3</sub> nanoparticles in a Silicon Xerogel Matrix. *Bull Russ Acad Sci Phys*. 2019;83(7):875–7.
- Ma J, Chen KZ. Silica-free hydrothermal synthesis of  $\epsilon$ -Fe<sub>2</sub>O<sub>3</sub> nanoparticles and their oriented attachment to nanoflakes with unique magnetism evolution. *Ceram Int*. 2018;44(16):19338–44.
- Ding Y, Morber JR, Snyder RL, Wang ZL. Nanowire structural evolution from Fe<sub>3</sub>O<sub>4</sub> to  $\epsilon$ -Fe<sub>2</sub>O<sub>3</sub>. *Adv Funct Mater*. 2007;17(7):1172–8.
- Gich M, Gazquez J, Roig A, Crespi A, Fontcuberta J, Idrobo JC, et al. Epitaxial stabilization of  $\epsilon$ -Fe<sub>2</sub>O<sub>3</sub> (001) thin films on SrTiO<sub>3</sub> (111). *Appl Phys Lett*. 2010;96:112508.
- Colomban PH, Sagon G. Vietnamese (15th Century) Blue-and-white, tam Thai and Lustre porcelains/stonewares: glaze composition and decoration techniques. *Archaeometry*. 2004;46(1):125–36.

22. Liu ZW, Zhang ZG, Li H, Wu W, Hua JJ, Cheng GF, Lin CC. Microstructure characteristics of the black-glazed shreds excavated from the Qingliangsi Kiln. *Key Eng Mater.* 2012;492:112–7.
23. Dejolie C, Sciau P, Li WD, Noé L, Mehta A, Chen K, et al. Learning from the past: rare  $\epsilon$ -Fe<sub>2</sub>O<sub>3</sub> in the ancient black-glazed Jian (Tenmoku) wares. *Sci Rep.* 2014;4:4941.
24. Xu YY, Qin Y, Ding F. Characterization of the rare oil spot glazed bowl excavated from the Xiao kiln site of north China. *Ceram Int.* 2017;43(12):8636–42.
25. Shen BL, Sciau P, Wang T, Brunet M, Li JM, Lu W, Zhu TQ. Micro-structural study of colored porcelains of Changsha kiln using imaging and spectroscopic techniques. *Ceram Int.* 2018;44(15):18528–34.
26. Liu Z, Jia C, Li L, Li XL, Ji LY, Wang LH, et al. The morphology and structure of crystals in Qing Dynasty purple-gold glaze excavated from the Forbidden City. *J Am Ceram Soc.* 2018;101(11):5229–40.
27. Wen R, Wang D, Wang LH, Dang YN. The colouring mechanism of the Brown glaze porcelain of the Yaozhou Kiln in the Northern Song Dynasty. *Ceram Int.* 2019;45(8):10589–95.
28. Wang T, Hole C, Ren Z, Zhang P, Shi P, Zhu JF, et al. Morphological and structural study of crystals in black-to-brown glazes of Yaozhou ware (Song dynasty) using imaging and spectroscopic techniques. *J Eur Ceram Soc.* 2021;41(12):6049–58.
29. Hoo QY, Wang XH, Sun Y, Hua QL, Cao XW, Song JH, Wen R. Formation mechanism of the pinholes in brown glazed stoneware from Yaozhou kiln. *Archaeometry.* 2021;64:644–54.
30. Wu B, Zhao WJ, Ren X, Liu XM, Li B, Feng SL, et al. Firing process and colouring mechanism of black glaze and brown glaze porcelains from the Yuan and Ming dynasties from the Qingliang Temple kiln in Baofeng, Henan. *China Ceram Int.* 2021;47(23):32817–27.
31. Hoo QY, Wang XH, Yuan F, Cao XW, Cao TW, Zhang ML. Microstructure and coloring mechanism of iron spots on bluish white porcelain from Jingdezhen of the Song Dynasty. *J Eur Ceram Soc.* 2021;41(6):3816–22.
32. Hoo QY, Liang YH, Yan XL, Wang XH, Cao TW, Cao XW. Millimeter-sized flower-like clusters composed of mullite and  $\epsilon$ -Fe<sub>2</sub>O<sub>3</sub> on the Hare's Fur Jian Ware. *J Eur Ceram Soc.* 2020;40(12):4340–7.
33. Kusano Y, Nakata H, Peng ZL, Maki RSS, Ogawa T, Fukuhara M. Studying and utilizing traditional technologies: microstructure and formation mechanism of  $\epsilon$ -Fe<sub>2</sub>O<sub>3</sub> on traditional Japanese Bizen Stoneware. *ACS Appl Mater Interfaces.* 2021;13(32):38491–8.
34. Wang LH, Wang Y, Zhang ML, Li QJ, Wu JM, Liu Z, et al. Three-dimensional microstructure of  $\epsilon$ -Fe<sub>2</sub>O<sub>3</sub> crystals in Ancient Chinese Sauce Glaze porcelain revealed by focused ion beam scanning electron microscopy. *Anal Chem.* 2019;91(20):13054–61.
35. Guan M, Kang BQ, Wei XJ, Li G, Jia C, Li H, et al. The microstructure of multicolor hare's fur glaze: the correlation between morphological and compositional characteristics and glaze color. *Herit Sci.* 2021;9:21.
36. Zheng JM. A short treatise on Deqing Kiln (德清窑略论). *Cult Relics.* 2011;07:50–60.
37. Shi L, Zhu JM. Origin of Celadon—Deqing Kiln (青瓷之源·德清窑). *Identif Appl Cult Relics.* 2011;08:58–66.
38. Zhu JM. Investigation of the proto-celadon kiln site in Deqing, Zhejiang (浙江德清原始青瓷窑址调查). *Archaeology.* 1989;09:779–88.
39. Kusano Y, Fukuhara M, Takada J, Doi A, Ikeda Y, Takano M. Science in the art of the master Bizen potter. *Acc Chem Res.* 2010;43(6):906–15.
40. Li QJ, Zhang ML, Wang LH, Yu YB, Xiong L, Zhou J, Yuan F. Analyzing the formation mechanism of 'Huoshihong' characteristics in the blue-and-white porcelain. *J Eur Ceram Soc.* 2022;42(15):7360–8.
41. Zhou R, Li JZ. The study of the body, glaze and firing technology of ancient ceramics produced in Jingdezhen (景德镇历代瓷器胎、釉和烧制工艺的研究). *Journal of the Chinese Ceramic Society.* 1960(02):49–63+97–98+103–105. <https://doi.org/10.14062/j.issn.0454-5648.1960.02.001>
42. Ding YZ, Li Y, Li H, Kang BQ, Hou JY, Wu JM. Study on application of thermal expansion method to determine firing temperature of black porcelain from Jian Kiln (热膨胀法判定建窑黑瓷烧成温度的应用研究). *China Ceramics.* 2021;57(1):60–5.
43. Colombari P. Full spectral range raman signatures related to changes in enameling technologies from the 18th to the 20th Century: guidelines, effectiveness and limitations of the Raman analysis. *Materials.* 2022;15(9):3158.
44. Froment F, Tournié A, Colombari P. Raman identification of natural red to yellow pigments: ochre and iron-containing ores. *J Raman Spectrosc.* 2008;39(5):560–8.
45. Tichane R. Ash Glazes. Iola, Wisconsin: Krause Publications; 1998.
46. Wang YL, Zheng JM. The Kilns Industry of the Zhejiang Area in the Sui and Tang Dynasties (隋唐时期浙江地区窑业的时空特征). *Southeast Culture.* 2015(02):82–88+135. <http://dnwh.njmuseum.com/file/pdf/2015/201502/20150211.pdf>
47. Yin M, Rehren T, Zheng JM. The earliest high-fired glazed ceramics in China: the composition of the proto-porcelain from Zhejiang during the Shang and Zhou periods (c. 1700–221 BC). *J Archaeol Sci.* 2011;38:2352–65.
48. Liu ZW, Zhang ZG, Wu W, Hua JJ, Ding MJ, Zhang CG, Li H. Glazing technology of Fujian black glaze of song dynasty (宋代福建黑釉的施釉工艺). *PTCA (Part A Phys Test).* 2011;47(04):212–6.
49. Jia C, Cui TJ, Yang JD. Scientific study on the stamped hard pottery unearthed from Niumiānshan Kiln Site in Xiaoshan, Hangzhou (杭州萧山牛面山窑址印纹硬陶的科技研究). *Cult Relics East.* 2014;02:87–92.

## Publisher's Note

Springer Nature remains neutral with regard to jurisdictional claims in published maps and institutional affiliations.

**Submit your manuscript to a SpringerOpen® journal and benefit from:**

- Convenient online submission
- Rigorous peer review
- Open access: articles freely available online
- High visibility within the field
- Retaining the copyright to your article

Submit your next manuscript at ► [springeropen.com](http://springeropen.com)